PCCP

PAPER

View Article Online
View Journal | View Issue

Cite this: *Phys. Chem. Chem. Phys.*, 2017, **19**, 24135

Co-assembly behaviour of Janus nanoparticles and amphiphilic block copolymers in dilute solution†

Qing Li, Liquan Wang* and Jiaping Lin*

Received 5th July 2017,
Accepted 11th August 2017

DOI: 10.1039/c7cp04501h

rsc.li/pccp

Nanoparticles can co-assemble with amphiphilic block copolymers (ABPs) in solution to generate nanoaggregates with unique properties, yet the mechanism of such a co-assembly behaviour for Janus nanoparticles (JPs) and ABPs remains unclear. Here, the self-assembly behaviour of JP/ABP mixtures in dilute solution was studied *via* theoretical simulations. Two kinds of ABPs with different volume fractions f_A of hydrophilic blocks were considered: one is symmetric copolymers with f_A = 0.5, and the other is asymmetric ABPs with f_A = 0.3. In the first case, mixtures of spheres and rods, connected networks and vesicles were formed sequentially as the volume fraction c_{JP} of nanoparticles increases. In the second case, vesicles were constantly formed. For both cases, at lower c_{JP} values, the nanoparticles were located at the core–corona interfaces. By contrast, at higher particle loadings, a large number of particles were involved in clusters embedded in the vesicle walls. Based on the simulation results, a morphological diagram in the space of c_{JP} and f_A was constructed to indicate the stability regions of different nanostructures. Specifically, it was found that the vesicles formed by JPs and ABPs with short hydrophilic blocks are stimuli-responsive. By changing the interaction parameters between hydrophobic blocks, controllable pores in the vesicle walls could be created. Our findings not only provide insights into the co-assembly behaviour of Janus nanoparticles and amphiphilic block copolymers in solution, but also offer a novel strategy to prepare nanoreactors with permeable membranes.

1. Introduction

Co-assembly of nanoparticles with amphiphilic block copolymers (ABPs) in selective solvents offers a bottom-up strategy to design and generate hybrid nanomaterials for applications in fluorescent probes,[1,2] magnetic resonance imaging devices,[3–5] drug delivery systems,[6] sensors and nonlinear optics,[7,8] and theranostic nanodevices,[9,10] *etc.* The aggregates formed by block copolymers, such as spherical micelles, rod-like micelles and vesicles, can serve as templates for the controllable organization of nanoparticles. These nanoparticles can be placed within the hydrophobic cores, within the hydrophilic coronas, or at the core–corona interfaces. Their spatial localization plays a critical role in determining the properties of hybrid aggregates.[11] Meanwhile, the incorporation of nanoparticles can also influence the supramolecular structures of parent copolymers. For example, Yang *et al.* investigated the co-assembly behaviour of poly(γ-benzyl-L-glutamate)-*b*-poly(ethylene glycol)-*b*-poly(γ-benzyl-L-glutamate) (PBLG-*b*-PEG-*b*-PBLG) triblock copolymers and Au nanoparticles in solution.[12] A morphological transition from spindle-like structures to vesicles could be observed when the nanoparticles were incorporated. Hickey *et al.* studied the morphologies of aggregates composed of magnetic nanoparticles and poly(acrylic acid)-*b*-polystyrene (PAA-*b*-PS) copolymers.[13] By tuning the solvent–nanoparticle and polymer–nanoparticle interactions, various nanostructures including hybrid vesicles, core–shell assemblies and spherical aggregates could be obtained.

Janus nanoparticles (JPs), which possess two physically or chemically distinct surface parts,[14] are well known because of their superior interfacial activity in comparison to homogeneous counterparts.[15] Their anisotropic nature allows for the integration of multiple functions into a single nanoparticle to produce multifunctional nanomaterials.[16–18] In addition, when decorated with surface patterns of specific attractive or repulsive interactions, they can self-assemble in solution into many intriguing superstructures,[19] such as one-dimensional nanowires,[20] two-dimensional free-standing membranes,[21] and three-dimensional Kagome lattices,[22] among others. For example, Shah *et al.* reported the actuation of self-limiting fibres of Janus ellipsoids

Shanghai Key Laboratory of Advanced Polymeric Materials, State Key Laboratory of Bioreactor Engineering, Key Laboratory for Ultrafine Materials of Ministry of Education, School of Materials Science and Engineering, East China University of Science and Technology, Shanghai 200237, China. E-mail: jlin@ecust.edu.cn, lq_wang@ecust.edu.cn

† Electronic supplementary information (ESI) available. See DOI: 10.1039/c7cp04501h

bearing opposite metal and polymeric surface parts.[20] By the application and removal of alternating-current electric fields, these fibrillary structures can elongate and relax reversibly, thus mimicking the behaviour of muscle fibres. Therefore, it is reasonable that the co-assembly of Janus nanoparticles and amphiphilic block copolymers in solution can also lead to hybrid aggregates that exhibit diverse morphologies and carry potential for various applications. However, limited by the difficulties in preparing Janus nanoparticles with defined structures on large scales, studies in this field are still in infancy.[14]

Over the past few years, many studies have demonstrated the power of theoretical simulations to reveal mechanisms behind natural and experimental processes and to guide future works.[23–25] As for the self-assembly of polymers and nanoparticles, a number of simulation techniques, including dynamic self-consistent field theory (DSCFT),[26] self-consistent field theory/density functional theory (SCFT/DFT),[27,28] Monte Carlo,[29] and molecular dynamics (MD),[30] have been proposed. Among these techniques, dissipative particle dynamics (DPD) is a mesoscopic simulation method based on the molecular dynamics (MD).[31] Its highly coarse-grained nature enables researchers to conduct simulations on much larger length and time scales in comparison to traditional MD-based techniques. Recently, the DPD method has been utilized to investigate the self-assembly behaviour of Janus nanoparticle/block copolymer mixtures in bulk.[32–34] Simulation results highly consistent with experimental observations have been obtained. For instance, Yan *et al.* conducted DPD simulations to study the self-assembly of diblock copolymers and Janus nanoparticles with different shapes (*e.g.*, Janus spheres, Janus cylinders and Janus discs).[32] For all cases, the Janus nanoparticles were located at the interfaces, with the opposite surface parts oriented toward their favoured polymeric phases, respectively. In addition, they demonstrated that the presence of Janus nanoparticles can significantly increase the viscosity of the nanoparticle/block copolymer composites, which implies a unique approach to tune the materials' processing properties. These works provided valuable insights into the self-assembly and spatial localization of Janus nanoparticles, and demonstrated the reliability of the DPD method for theoretical investigations. So far, most existing reports were concerned with the JP/block copolymer mixtures in bulk, yet less attention has been paid to the underlying principles governing the formation of JP/ABP hybrid aggregates in dilute solution. However, understanding these principles is of great significance to guide the exploration of novel microstructures with potential nanotechnological applications. In this regard, the DPD method could be a useful tool to illuminate the factors influencing the morphologies and structures of JP/ABP nanoaggregates in solution, as well as to elaborate the underlying mechanisms.

In the present work, the self-assembly behaviour of Janus nanoparticle/amphiphilic block copolymer mixtures in selective solvents was studied using DPD simulations. The effects of the copolymer composition and the nanoparticle loading were examined. The spatial localizations of nanoparticles at the core–corona interfaces were quantitatively characterized. The mechanisms behind the morphological transitions of aggregates and the shifted distributions of nanoparticles were discussed. In addition, it was found that, by changing the interaction parameters between hydrophobic blocks, controllable pores can be created in the walls of vesicles formed by copolymers with short hydrophilic blocks. This finding suggests a novel strategy to design intelligent nanoreactors which can selectively permit the translocation of agents with different sizes across the membranes.

2. Methods and models

Dissipative particle dynamics (DPD) is a particle-based, mesoscopic simulation method.[31] In DPD simulations, the momentum is conserved and the hydrodynamics can be preserved. Details of the DPD method and its advantages can be found in our previous works and literature.[25,31,35,36] Here, only a brief description is given. In the DPD method, each bead represents a lump of atomic or molecular matter, which interacts with one another *via* a soft repulsive potential. The movement of each bead is governed by the equations of motion:

$$\frac{\mathrm{d}\mathbf{r}_i}{\mathrm{d}t} = \mathbf{v}_i, \quad m_i\frac{\mathrm{d}\mathbf{v}_i}{\mathrm{d}t} = \mathbf{f}_i \tag{1}$$

where t is the time; m_i is the mass of the ith beads; $\mathbf{r}_i$ and $\mathbf{v}_i$ are the position and velocity of the ith bead, respectively; and $\mathbf{f}_i$ is the force applied on it. In the present study, the masses of beads were set to be identical. $\mathbf{f}_i$ consists of four parts, *i.e.*, a conservative force $\mathbf{F}_{ij}^{\mathrm{C}}$, a dissipative force $\mathbf{F}_{ij}^{\mathrm{D}}$, a random force $\mathbf{F}_{ij}^{\mathrm{R}}$, and a spring bond force $\mathbf{F}_{ij}^{\mathrm{S}}$:

$$\mathbf{f}_i = \sum_{j\neq i}\left(\mathbf{F}_{ij}^{\mathrm{C}} + \mathbf{F}_{ij}^{\mathrm{D}} + \mathbf{F}_{ij}^{\mathrm{R}} + \mathbf{F}_{ij}^{\mathrm{S}}\right) \tag{2}$$

The conservative force $\mathbf{F}_{ij}^{\mathrm{C}}$ is a soft repulsive interaction vanishing at a critical distance r_{c}:

$$\mathbf{F}_{ij}^{\mathrm{C}} = a_{ij}\sqrt{\omega^{\mathrm{C}}(r_{ij})}\hat{\mathbf{r}}_{ij} \tag{3}$$

where a_{ij} is the maximum repulsion between the ith and jth beads; $\mathbf{r}_{ij} = \mathbf{r}_i - \mathbf{r}_j$; $r_{ij} = |\mathbf{r}_{ij}|$; $\hat{\mathbf{r}}_{ij} = \mathbf{r}_{ij}/r_{ij}$; and $\omega^{\mathrm{C}}(r_{ij})$ is a weighting function, reading as:

$$\omega^{\mathrm{C}}(r_{ij}) = \begin{cases} (1 - r_{ij}/r_{\mathrm{c}})^2, & (r_{ij} < r_{\mathrm{c}}) \\ 0, & (r_{ij} \geq r_{\mathrm{c}}) \end{cases} \tag{4}$$

In this study, r_{c} is used as the unit of distance. The dissipative force $\mathbf{F}_{ij}^{\mathrm{D}}$ is dependent on the relative velocities of beads, given by:

$$\mathbf{F}_{ij}^{\mathrm{D}} = -\gamma\omega^{\mathrm{D}}(r_{ij})(\hat{\mathbf{r}}_{ij}\cdot\mathbf{v}_{ij})\hat{\mathbf{r}}_{ij} \tag{5}$$

and the random force $\mathbf{F}_{ij}^{\mathrm{R}}$ is defined by:

$$\mathbf{F}_{ij}^{\mathrm{R}} = \mu\omega^{\mathrm{R}}(r_{ij})\Gamma_{ij}\Delta t^{-1/2}\hat{\mathbf{r}}_{ij} \tag{6}$$

where γ and μ are the friction coefficient and the noise amplitude, respectively; $\mathbf{v}_{ij} = \mathbf{v}_i - \mathbf{v}_j$; $\omega^{\mathrm{D}}(r_{ij})$ and $\omega^{\mathrm{R}}(r_{ij})$ are two weighting functions vanishing at $r = r_{\mathrm{c}}$; and Γ_{ij} is a randomly fluctuating variable obeying the Gaussian statistics:

$$\langle\Gamma_{ij}(t)\rangle = 0, \quad \langle\Gamma_{ij}(t)\Gamma_{kl}(t')\rangle = (\delta_{ik}\delta_{jl} + \delta_{il}\delta_{jk})\delta(t - t') \tag{7}$$

Groot and Warren argued that the following relation must be satisfied:[31]

$$\omega^{D} = [\omega^{R}(r_{ij})]^2 = \omega^{C}(r_{ij}) \quad (8)$$

and the values of γ and μ should be coupled by:

$$\mu^2 = 2\gamma k_B T \Delta t \quad (9)$$

where k_B is the Boltzmann constant and T is the absolute temperature. By this means, equilibrium states corresponding to the canonical ensemble (NVT) can be achieved. Additionally, the spring force $\mathbf{F}_{ij}^{S}$ should be considered for the DPD beads within the block copolymers.[37] It takes the following form:

$$\mathbf{F}_{ij}^{S} = C(1 - r_{ij}/r_{eq})\hat{\mathbf{r}}_{ij} \quad (10)$$

where C is the spring constant and r_{eq} is the equilibrium distance. Here we chose $C = 30k_BT/r_c$ and $r_{eq} = 0.86r_c$ based on our previous works.[12,38] The reduced units were adopted for all physical quantities. The units of time, length, mass and energy are defined by τ, r_c, m and k_BT, respectively. The time unit τ can be obtained by $\tau = (mr_c^2/k_BT)^{1/2}$. The γ and μ values are set to be $4.5k_BT\tau/r_c^2$ and $3.0k_BT\tau/r_c$, respectively.[37,39] The equations of motion (eqn (1)) were integrated by a modified velocity-Verlet algorithm, and the time step Δt was set to be 0.02τ.[31]

The coarse-grained model of the Janus nanoparticles studied in the present work is shown in Fig. 1a. Each model particle involves six hydrophilic beads (denoted by J_A) and six hydrophobic beads (denoted by J_B) restricted to move together as an intact rigid body. The radius R_{JP} of model particles was set to be $0.5r_c$. Such a close packing is sufficient to avoid the possible penetration of solvent and copolymer beads into the nanoparticles (for evidence, see Fig. S2, ESI†). It should be noted that the surface roughness of Janus nanoparticles could influence the self-assembly structures. The smoother surfaces can be achieved by packing the twelve DPD beads closer, while the rougher surfaces can be obtained by packing the twelve DPD beads looser. However, our model can only be constructed by closely packing the twelve DPD beads together to prevent the penetration of solvent and copolymer beads. Therefore, it is hard to examine the effect of surface roughness in the present work. The coarse-grained model of amphiphilic block copolymers contains l_A hydrophilic beads (denoted by A) and l_B hydrophobic beads (denoted by B). The harmonic spring potential was used to connect adjacent beads (see eqn (10)). The number of beads within each model copolymer was fixed to be 10 ($l_A + l_B = 10$). The composition f_A of copolymers is defined as the volume fraction of hydrophilic blocks: $f_A = l_A/(l_A + l_B)$. We have calculated the radius R_g of gyration for model copolymers (for method, see the ESI†). The result ($R_g \approx 2.05r_c$) suggests that the size of Janus nanoparticles is very small as compared to the block copolymers. If we consider a typical block copolymer with $R_g \approx 20$ nm, the Janus nanoparticles studied in the present work would be around 10 nm in diameter. Over the past few years, only a small number of research studies were reported on the synthesis of small Janus nanoparticles with a diameter of around 10 nm.[40] On the other hand, if the studied block copolymers are considered to be with a high molecular weight, the size of Janus nanoparticles in the present work can be as large as 30–40 nm, which is comparable to the size of the Janus nanoparticles synthesized by Müller *et al.*[41] Therefore, the present models can be regarded as either the case of small Janus nanoparticles or the case of high-molecular-weight copolymers and large Janus nanoparticles, which can be found in the experiments. The solvents (denoted by S) are modelled as individual DPD beads. They are favoured by the J_A and A beads. The volume fractions of JPs, ABPs and solvents were denoted by c_{JP}, c_{ABP} and c_{sol}, respectively.

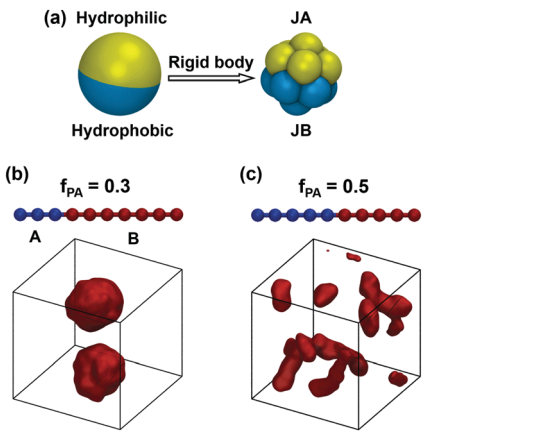

Fig. 1 (a) Coarse-grained model of the Janus nanoparticles (JPs). Each model particle contains equally-sized hydrophilic (J_A) and hydrophobic (J_B) parts. (b and c) Coarse grained model of amphiphilic block copolymers (ABPs) with composition (b) f_A = 0.3 and (c) f_A = 0.5. Each model copolymer contains a hydrophilic block (A) and a hydrophobic block (B). Aggregates formed by corresponding copolymers are also shown. Hydrophobic cores of aggregates are coloured in red. Solvents and hydrophilic coronas are not shown for clarity.

The simulations were all conducted in cubic boxes with the periodic boundary conditions imposed on three directions (x, y and z). Usually, the box size was set as $L = 30r_c$. We have checked the influence of the box size on the self-assembly structures to remove the finite size effect and unphysical results. When a large number of aggregates are formed in the simulation box, the box size has a less marked effect on the self-assembly structures. However, for boxes with only a small number of aggregates included, the box size could have a pronounced effect on the self-assembly structures. For example, in large boxes ($L = 30r_c$ and $L = 40r_c$), the block copolymers and nanoparticles tend to form vesicles as the composition of copolymers is $f_A = 0.5$ and the volume fraction of nanoparticles is $c_{JP} = 0.6$ (see Fig. 2e). However, such vesicles cannot be obtained if the simulation box is too small, *e.g.*, $L = 20r_c$. Instead, membranes spanning the entire box can be observed. Therefore, we have paid special attention to the above cases, and have varied the box size to obtain the physical results. The total number of DPD beads was fixed to be 81 000 usually. The NVT ensemble was adopted, and the k_BT was fixed to be constant ($k_BT = 1.0$). The interaction parameters between different DPD beads are listed in Table 1. They are defined so as to reproduce the segregation between the solvophobic parts (J_B and B) and the solvophilic parts (J_A and A). The following

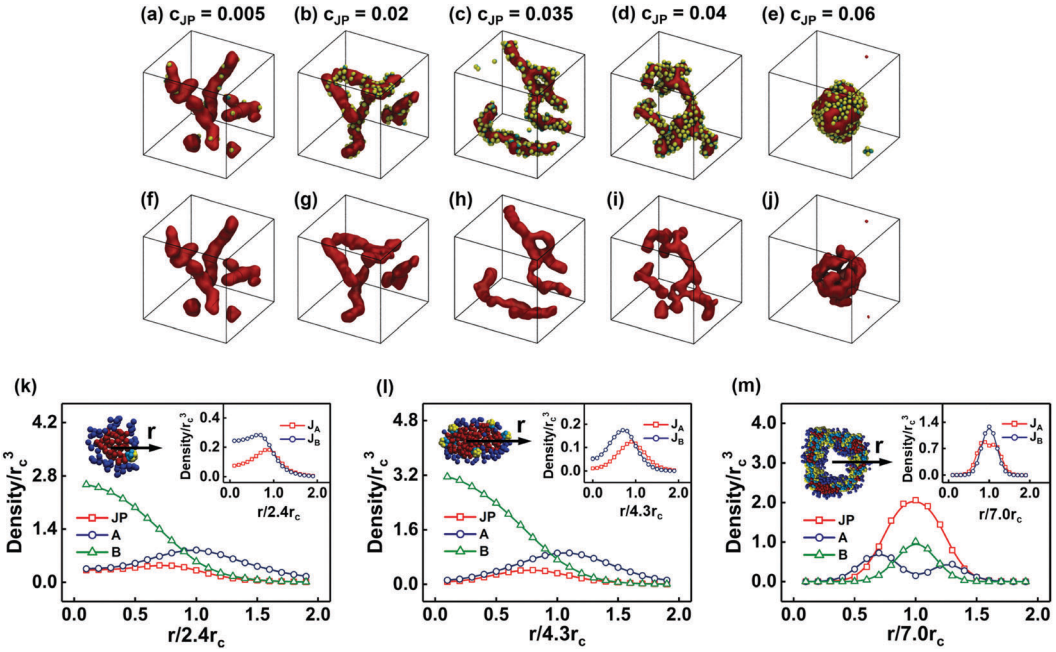

Fig. 2 (a–j) Snapshots of JP/ABP aggregates formed at various c_{JP}: (a and f) c_{JP} = 0.005; (b and g) c_{JP} = 0.02; (c and h) c_{JP} = 0.035; (d and i) c_{JP} = 0.04; (e and j) c_{JP} = 0.06. Composition f_A of copolymers was fixed to be 0.5. JPs are schemed into spheres with two equally-sized J_A (yellow) and J_B (blue) hemispheres. Structures of B blocks are coloured in red and displayed at the second row. Blocks A and solvents are omitted for clarity. (k–m) One-dimensional density profiles along the *r*-arrows for (k) a spherical micelle formed at c_{JP} = 0.005, (l) a rod-like micelle formed at c_{JP} = 0.02, and (m) a vesicle formed at c_{JP} = 0.06. Insets at the upper right corners show the density profiles of J_A and J_B beads. Cross-sections of aggregates are displayed at the upper left corners. J_A, J_B, A and B beads are coloured in yellow, cyan, blue and red, respectively.

simulation procedures were adopted. At the beginning, all of the components (JPs, ABPs and solvents) were randomly placed in the box. The interaction parameters were all set to be 25, and a preliminary simulation was conducted for 10^4 time steps to fully homogenize the system. Then, the unfavourable interactions between dislike components were turned on (see Table 1), and the simulation was conducted for another 8×10^5 time steps. This duration is sufficient for the equilibrium state to be achieved.[37,42] The vesicles with controllable pores were obtained by first choosing several hybrid vesicles formed at c_{JP} = 0.3 and f_A = 0.3 as the initial structures, followed by resetting the interaction parameter a_{BB} from 25 to 25 − Δa, where Δa is a positive value whose magnitude can be related to the attractive interactions among hydrophobic blocks. The simulation was conducted for at least 3×10^5 time steps.

3. Results and discussion

It is well-known that the morphologies of amphiphilic block copolymer (ABP) aggregates are determined by the composition of copolymers.[43] "Star-like" aggregates (*e.g.*, spherical and rod-like micelles) can be formed when the length of hydrophilic blocks is comparable to or slightly larger than that of hydrophobic blocks, while block copolymers whose hydrophilic blocks are much shorter than the hydrophobic blocks tend to form "crew-cut" structures (such as vesicles and large compound micelles). Considering this, we decided to focus on two representatives, *i.e.*, symmetric ABPs with equally-sized hydrophilic and hydrophobic blocks (f_A = 0.5) and asymmetric ABPs with shorter hydrophilic blocks (f_A = 0.3). In order to elucidate the co-assembly behaviour of JPs and ABPs in dilute solution, we fixed the volume fraction c_{sol} of solvents to be 0.9, and varied the volume fraction c_{JP} of nanoparticles in the range from 0 to 0.06.

Table 1 Interaction parameters a_{ij} (in DPD units) used in the present work

	J_A	J_B	A	B	S
J_A	25	75	25	75	25
J_B		25	75	25	75
A			25	75	25
B				25–20	75
S					25

3.1 Symmetric ABPs with f_A = 0.5

Aggregate morphologies and structures. In this subsection, the co-assembly behaviour of Janus nanoparticles and amphiphilic block copolymers with f_A = 0.5 is elaborated. As shown in Fig. 1b, these copolymers tend to form dispersed spherical and rod-like aggregates when the nanoparticles are absent. This is consistent with the morphologies of micelles obtained in experiments.[43] Fig. 2a–j show the morphologies of JP/ABP hybrid aggregates formed at various c_{JP}. At lower c_{JP} values (Fig. 2a and b), mixtures of spheres and rods were formed. The particles are exclusively located at the surface of B domains, with their J_B and J_A parts oriented toward the aggregate cores and coronas, respectively. As c_{JP} increases from 0.005 to 0.04 (Fig. 2a–d), the

rod-like micelles become elongated and interconnected into networks while the spherical micelles gradually disappear. The skeletons of networks are composed of the hydrophobic blocks (see Fig. 2f–i), with the nanoparticles distributed at the core–corona interfaces. When c_{JP} is further increased, a dramatic morphological change from networks to vesicles can be observed (Fig. 2e and j). The B domains coexist with the nanoparticle aggregates, with only a small portion of particles located at the interfaces.

We further analysed the structures of aggregates by plotting the density profiles of respective components (Fig. 2k–m). The density φ_α of component α is defined as the number of beads in a unit volume.[37] Fig. 2k shows the density distributions of JP beads (φ_{JP}), hydrophilic blocks (φ_A) and hydrophobic blocks (φ_B) within a spherical micelle formed at $c_{JP} = 0.005$. It can be viewed that the aggregate cores and coronas are rich in the hydrophobic and hydrophilic blocks, respectively. The peak of φ_{JP} is located between the peaks of φ_A ($r \approx 2.4r_c$) and φ_B ($r = 0r_c$), which is consistent with the interfacial distribution of nanoparticles. We also plotted the profiles of φ_{J_A} and φ_{J_B} in the inset of Fig. 2k. The peaks of φ_{J_A} and φ_{J_B} are proximate to the peaks of φ_A and φ_B, respectively, which confirms the orientation of J_A and J_B hemispheres toward their favoured blocks. The density profiles for the rod-like micelle formed at $c_{JP} = 0.02$ (Fig. 2l) are analogous to those shown in Fig. 2k, which suggests similar structures of spherical and rod-like micelles.

Fig. 2m shows the density profiles of a hybrid vesicle formed at $c_{JP} = 0.06$. The profiles of φ_A and φ_B exhibit bimodal and unimodal features, respectively, which are a typical character of vesicles. The remarkable peak of φ_{JP} overlapped with the peak of φ_B and sandwiched by the peaks of φ_A confirms the coexistence of copolymer and nanoparticle domains within the vesicle walls. It is worth noting that the profiles of φ_{J_A} and φ_{J_B} exhibit bimodal and unimodal features, respectively (see the inset of Fig. 2m), which implies the bilayer-like structure of JP clusters.

Particle position. In order to obtain detailed knowledge on the spatial localization of Janus nanoparticles at the core–corona interfaces, we calculated the fraction $f_{w(core)}$ of the nanoparticle surface wrapped by the hydrophobic blocks for particles within the spherical and rod-like micelles. This parameter has been utilized by Yan *et al.* to characterize the localization of Janus particles within block copolymer scaffolds.[44] As illustrated in Fig. 3a–c, $f_{w(core)} = 0.5$ indicates that the nanoparticle is exactly anchored at the interface, whereas $f_{w(core)} < 0.5$ and $f_{w(core)} > 0.5$ indicate that the nanoparticle is shifted toward the corona and the core, respectively. Fig. 3d–g show the distributions of $f_{w(core)}$ and the best-fitted Gaussians at various particle loadings. The number-average wrapping fraction $\bar{f}_{w(core)}$ and the variance σ^2 which is related to the width of distributions are also shown. It can be viewed that for all c_{JP} values, $f_{w(core)}$ of the most nanoparticles are smaller than 0.5, which signifies a prevalent shift toward the coronas and solvents. This shifted distribution can be explained in terms of the dimensionless interfacial energy $g(\theta)$, where θ is the

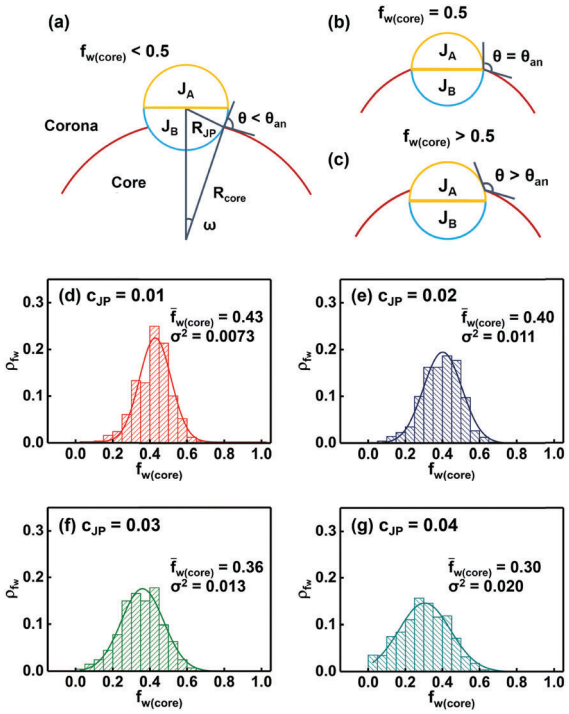

Fig. 3 (a–c) Schematic illustrations of JPs with different $f_{w(core)}$ located at core–corona interfaces: (a) $f_{w(core)} < 0.5$, (b) $f_{w(core)} = 0.5$, (c) $f_{w(core)} > 0.5$. Radii of the particle and the aggregate are denoted by R_{JP} and R_{core}, respectively. Contact angle θ corresponding to the "anchoring" position ($f_{w(core)} = 0.5$) is denoted by θ_{an}. J_A and J_B hemispheres are coloured in yellow and cyan, respectively. Core–corona interfaces are coloured in red. (d–g) Volume fractions ρ_{fw} of JPs with various $f_{w(core)}$ at increasing c_{JP}: (d) $c_{JP} = 0.01$, (e) $c_{JP} = 0.02$, (f) $c_{JP} = 0.03$, and (g) $c_{JP} = 0.04$. Composition of ABPs was fixed to be $f_A = 0.5$. Solid lines show the best-fitted Gaussians. Number-average wrapping fraction $f_{w(core)}$ and variance σ^2 are displayed.

contact angle, for a symmetrical Janus sphere located at the core–corona interface of a spherical micelle, which is given by:[45]

$$g_B(\theta) = \gamma_B[\cos(\theta - \omega)] - \frac{1 - \cos^3\omega}{3\varepsilon^2} - \frac{\varepsilon}{3}[3\cos(\theta - \omega) - \cos^3(\theta - \omega)] \quad (11)$$

for $0 \le \theta \le \theta_{an}$, and

$$g_A(\theta) = \gamma_A[\cos(\theta - \omega)] - \frac{1 - \cos^3\omega}{3\varepsilon^2} - \frac{\varepsilon}{3}[3\cos(\theta - \omega) - \cos^3(\theta - \omega)] \quad (12)$$

for $\theta_{an} \le \theta \le \pi$, where $\varepsilon = R_{JP}/R_{core}$ is the curvature of the interface; R_{JP} and R_{core} are the radii of the nanoparticle and the aggregate core, respectively; $\theta_{an} = \pi/2 + \arcsin\varepsilon$ is the contact angle corresponding to the anchoring position (see Fig. 3b); $\omega = \arctan[\varepsilon\sin\theta/(1 + \varepsilon\cos\theta)]$ is the central angle (see Fig. 3a); $\gamma_A = (\sigma_{AJ_A} - \sigma_{BJ_A})/\sigma_{AB}$; and $\gamma_B = (\sigma_{AJ_B} - \sigma_{BJ_B})/\sigma_{AB}$ ($\sigma_{\alpha\beta}$ is the interfacial tension between the components α and β). The subscripts A and B stand for the cases where the particle is shifted toward the core (Fig. 3c) and the corona (Fig. 3a), respectively. We plotted the dependence of $g(\theta)$ on the contact angle θ at various values of ε, which is shown in the ESI† (see Fig. S1). It can

be viewed that, for highly curved interfaces ($\varepsilon > 0.2$), the contact angle θ_m corresponding to the minimal interfacial energy is always smaller than the anchoring angle θ_{an}. In order to minimize the interfacial energy, the nanoparticles have to adopt a shifted distribution with $\theta < \theta_{an}$ and $f_{w(core)} < 0.5$ toward the solvent (see Fig. 3a). In the present work, R_{JP} is $0.5r_c$, and the radius of spherical micelles at very small c_{JP} values is around $2.4r_c$ ($c_{JP} = 0.05$; see Fig. 2k). This leads to $\varepsilon = 0.21$. As c_{JP} rises, the volume fraction c_{ABP} decreases (the volume fraction c_{sol} of the solvent is fixed to be 0.9 in the present work), and the radius of spherical and cylindrical micelles is reduced. As a result, the curvature ε of aggregate cores becomes larger than 0.2, and the shifted distribution toward the coronas is energetically favoured. (For details, see the ESI.†)

It can also be viewed from Fig. 3d–g that an increase in c_{JP} results in broader distributions of $f_{w(core)}$ and smaller values of $\bar{f}_{w(core)}$. On one hand, the increase in c_{JP} is accompanied by the decrease in c_{ABP}, since the volume fraction of the solvent is fixed in our simulations. Therefore, the contact probability of neighbour nanoparticles rises, which leaves behind many nanoparticles with small $f_{w(core)}$. This effect results in smaller $\bar{f}_{w(core)}$ and broader distributions of $f_{w(core)}$. On the other hand, the drop in c_{ABP} leads to the formation of spherical and rod-like aggregates with a smaller core radius and hence a larger curvature of interfaces. As shown in Fig. S1e (ESI†), this enlarges the absolute value of the difference between θ_m and θ_{an}. Consequently, the shift of nanoparticles becomes stronger and the value of $\bar{f}_{w(core)}$ is reduced.

Morphological transition. As stated above, a morphological transition from dispersed spherical and rod-like micelles to interconnected networks and to vesicles can be triggered by an increase in the volume fraction c_{JP} of nanoparticles. In order to characterize this morphological change, we calculated the volume distributions of aggregates at various c_{JP} with the periodic boundary conditions taken into account. In the present work, every simulation system actually involves an infinite number of identical boxes called images. For each system, we constructed an "enlarged" box composed of N images (see the insets of Fig. 4a–c), and calculated the volume of each aggregate within it (for method, see the literature[46]). Fig. 4a–c shows the volume distributions of spheres and rods formed at $c_{JP} = 0.01$, networks formed at $c_{JP} = 0.035$, and vesicles formed at $c_{JP} = 0.06$, respectively. The number of images in each enlarged box is set to be $N = 8$. It can be found from Fig. 4a and b that the volumes of dispersed aggregates are at least an order of magnitude smaller than those of networks ($10^{2.5-4}V_0$ *vs.* $10^{4-5.5}V_0$, where V_0 is the volume occupied by a single DPD bead), which is consistent with the dispersive nature of spheres/rods and the continuous nature of networks. The volumes of vesicles ($10^{3.5-4}V_0$; Fig. 4c) are less than the volumes of networks and comparable to those of dispersed rod-like micelles. The narrow distribution can be attributed to the fact that, for each system, only one vesicle can be formed. Based on the volume distributions of aggregates, we calculated the number-average volume $\bar{V}$ of aggregates at various c_{JP}. The results are shown in Fig. 4d. The values of $\bar{V}$ exhibit little change at small c_{JP} values and increase dramatically

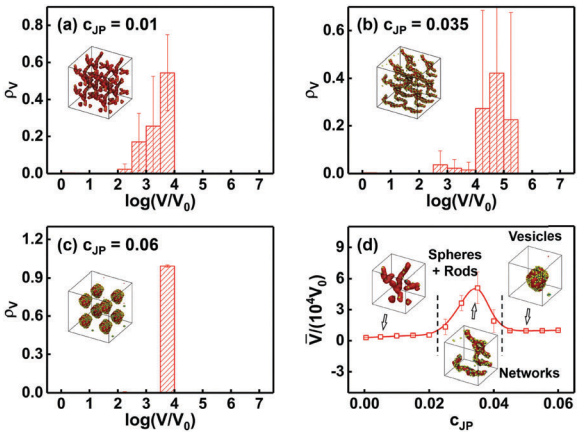

Fig. 4 (a–c) Volume distributions ρ_V of aggregates formed at different c_{JP}: (a) $c_{JP} = 0.01$, (b) $c_{JP} = 0.035$, (c) $c_{JP} = 0.06$. V_0 is the volume occupied by a single DPD bead. Insets show the snapshots of typical aggregates. (d) Number-average volume $\bar{V}$ of aggregates as the function of c_{JP}. Snapshots of aggregates at corresponding c_{JP} are displayed. Stability regions of different structures are separated by dashed lines.

for $c_{JP} > 0.02$. This behaviour is in accordance with the interconnection of aggregates into networks. The value of $\bar{V}$ quickly falls to $\sim 10^{3.5}V_0$ when the particle volume fraction c_{JP} is further increased beyond 0.04, which is consistent with the appearance of vesicles. Therefore, the stability regions of different structures can be separated, and the boundaries are shown in Fig. 4d.

The transition from dispersed micelles to networks can be related to the following effects. In the absence of nanoparticles, the symmetric block copolymers within the spherical and rod-like micelles adopt a cone-like shape to minimize the interfacial area, and the coalescence of aggregates is prevented by the steric effect of hydrophilic blocks. The introduction of nanoparticles leads to (1) reduced interfacial tension which favours the formation of aggregates with a larger surface area, and (2) weakened repulsive interaction of hydrophilic blocks due to the decreased c_{ABP} and the steric effect of Janus nanoparticles located at the interfaces. These effects facilitate the formation of networks instead of dispersive spheres and rods.

As for the transition from networks to vesicles, the underlying mechanism can be explained as follows. It has been demonstrated that the spatial distribution of nanoparticles in block copolymer scaffolds is determined by their relative sizes. When the radius of particles is smaller than the radius of gyration R_g of copolymers, the random distribution is favoured. In this circumstance, the particles can be fully wrapped by the polymer chains, and the behaviour of the system is governed by the translational entropy of nanoparticles.[47] In contrast, nanoparticles whose radius is much larger than R_g of copolymers are expelled from the matrix to maximize the conformational entropy of copolymers.[28] In the present study, R_{JP} ($0.5r_c$) is smaller than R_g ($\sim 2.05r_c$) of model copolymers, and the sizes of J_A and J_B hemispheres are also smaller than R_g of hydrophilic blocks ($\sim 1.11r_c$) and hydrophobic blocks ($\sim 1.09r_c$), respectively. (For details on the calculation of R_g, see the ESI.†) All of these effects favour the random distribution of nanoparticles

at the core–corona interfaces at lower c_{JP} values. However, at higher particle loadings, the space for each block to move within is highly limited if such a random distribution is still adopted. As a result, the nanoparticles and copolymers tend to microphase-separate to lower the conformational entropy of copolymer chains. The amphiphilic nature of Janus nanoparticles leads to the formation of bilayer-like structures, which are combined with copolymer domains to form vesicles.

3.2 Asymmetric ABPs with f_A = 0.3

In this subsection, we turn to study the co-assembly behaviour of Janus nanoparticles (JPs) and amphiphilic block copolymers (ABPs) whose hydrophilic blocks are shorter than the hydrophobic blocks. These copolymers can form ''crew-cut'' aggregates (such as vesicles and large compound micelles) in solution. Here, the self-assembly behaviour of copolymers with f_A = 0.3 are elaborated in detail, while the behaviours of copolymers with other compositions are briefly described. As shown in Fig. 1c, the ABPs with f_A = 0.3 can aggregate into vesicles, which is consistent with experimental observations.[43] The volume fraction c_{sol} of solvents was fixed to be 0.9, and the volume fraction c_{JP} of Janus nanoparticles was increased from 0 to 0.06.

Aggregate morphologies and structures. Fig. 5 shows the morphologies of aggregates formed by the mixtures of JPs and ABPs with increasing c_{JP}. It can be observed that vesicles are constantly formed. However, these vesicles exhibit diverse structures. As shown in Fig. 5a (c_{JP} = 0.01) and Fig. 5b (c_{JP} = 0.02), the vesicle cores are composed of hydrophobic blocks with the nanoparticles distributed at the surfaces of B domains. The B structures are free of rips or holes (see Fig. 5e and f). As c_{JP} increases to 0.04 (Fig. 5c and g), aggregates of nanoparticles embedded in the B domains can be observed. Meanwhile, a large number of particles are still located at the interfaces. At even higher particle loadings (Fig. 5d, c_{JP} = 0.06), separated B domains and nanoparticle aggregates within the vesicle walls were formed. Only a small portion of particles is still located at the core–corona interfaces.

The structures of vesicles formed at various particle loadings (c_{JP}) were further characterized by using the density profiles of components. Fig. 5i displays the profiles for a hybrid vesicle formed at c_{JP} = 0.02. The curve of φ_{JP} exhibits two peaks, each of which is sandwiched by the φ_B peak and a φ_A peak. This is consistent with the interfacial distribution of nanoparticles. The curves of φ_{J_A} and φ_{J_B} both exhibit bimodal features (see the inset), and the peaks of φ_{J_B} are closer to the centre of the vesicle wall than those of φ_{J_A}. This confirms the ordered orientation of nanoparticles. With c_{JP} increasing from 0.02 to 0.04, the two peaks of φ_{JP} become stronger and interfere with each other (see Fig. 5j). At the same time, the two peaks of φ_{J_A} are also interfered, and only one φ_{J_B} peak remains. These observations are consistent with the formation of bilayer-like structures of nanoparticles within the vesicle walls.

Further increasing c_{JP} to 0.06 leads to much weaker φ_A and φ_B peaks (see Fig. 5k) than those shown in Fig. 5i and j. Meanwhile, a distinctive peak of φ_{JP} overlapped with the peak of φ_B and sandwiched by the peaks of φ_A appears. This is consistent with the coexistence of JP aggregates and B domains

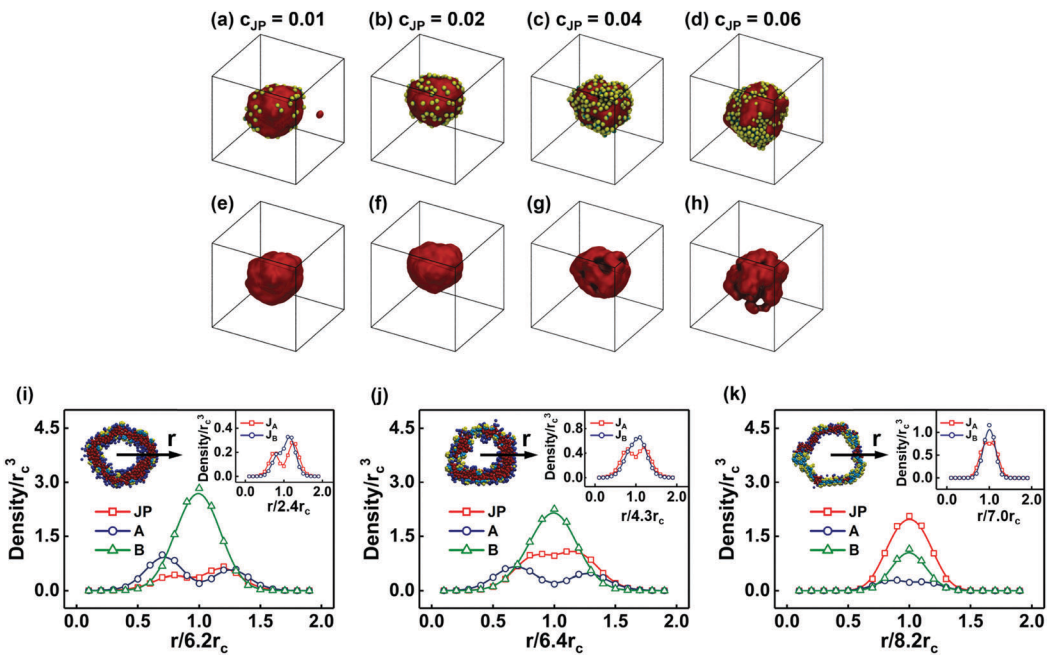

Fig. 5 (a–h) Snapshots of JP/ABP aggregates formed at various c_{JP}: (a and e) c_{JP} = 0.01; (b and f) c_{JP} = 0.02; (c and g) c_{JP} = 0.04; (d and h) c_{JP} = 0.06. Composition f_A of copolymers was fixed to be 0.3. JPs are schemed into spheres with two equally-sized J_A (yellow) and J_B (blue) hemispheres. Structures of B blocks are coloured in red. Blocks A and solvents are omitted for clarity. (i–k) One-dimensional density profiles along the r-arrows for vesicles formed at (i) c_{JP} = 0.02, (j) c_{JP} = 0.04 and (k) c_{JP} = 0.06. Insets at the upper right corners show the density profiles of J_A and J_B beads. Cross-sections of aggregates are displayed at the upper left corners. J_A, J_B, A and B beads are coloured in yellow, cyan, blue and red, respectively.

within the vesicle walls. The profile of φ_{J_B} shows an individual peak sandwiched by two φ_{J_A} peaks, which confirms the bilayer-like feature of JP aggregates (see the inset of Fig. 5k). The formation of separated particle aggregates and B domains can be ascribed to the conformational entropy of copolymer chains which has been discussed in the last subsection. The structure of the present vesicle is similar to that shown in Fig. 2m except for a larger radius ($\sim 8.2r_c$ *vs.* $\sim 7.0r_c$).

Particle position. We further used the fraction $f_{w(core)}$ of the particle surface wrapped by the hydrophobic blocks to characterize the spatial localization of Janus nanoparticles at the core–corona interfaces of hybrid vesicles (for the relation between the value of $f_{w(core)}$ and the position of nanoparticles, see Fig. 3a–c). Fig. 6 shows the distributions of the wrapping fraction $f_{w(core)}$ for nanoparticles within the vesicles formed at lower particle loadings. The solid curves represent the best-fitted Gaussians. The number-average wrapping fraction $\bar{f}_{w(core)}$ and the variance σ^2 are also displayed. For all particle loadings, the wrapping fraction $f_{w(core)}$ of the most particles are smaller than 0.5, which implies a prevalent shift toward the coronas. Comparing the distributions shown here with those displayed in Fig. 3, one can find that the increase in c_{JP} from 0.01 to 0.03 barely influences the values of $\bar{f}_{w(core)}$ but only leads to a broadening in the distributions of $f_{w(core)}$ (see Fig. 6a–c). The insensitivity of $\bar{f}_{w(core)}$ to c_{JP} can be attributed to the smaller curvature of the vesicle interfaces compared with those of spherical and rod-like micelles. The wider distributions of $f_{w(core)}$ are due to the increased contact probability of neighbouring nanoparticles with decreasing c_{ABP} (for detail, see the last subsection). At even higher particle loadings, the phase separation of nanoparticles and copolymers leads to an obvious decrease in $\bar{f}_{w(core)}$ and a further broader distribution of $f_{w(core)}$, which can be viewed from Fig. 6d.

Controllable pores. As stated above, we observed a special kind of aggregates formed by Janus nanoparticles and amphiphilic block copolymers, *i.e.*, the vesicles with defective B structures and embedded nanoparticle clusters (see Fig. 5c and g). Moreover, we found that the structures of these vesicles can be responsive for external stimulations, such as changes in temperature or pH. This feature can be utilized to construct "smart" nanoreactors for applications in enzyme catalysis, polymerization, nanoparticle synthesis, and artificial organelles.[48] In experiments, such responsive vesicles can be produced by introducing stimuli-responsive components, such as temperature-responsive poly(*N*-isopropyl acrylamide) (PNIPAAm) or pH-responsive poly(styrene boronic acid) (PSBA), into the vesicles.[48] In DPD simulations, changes in the environmental conditions can be realized by varying the interaction parameters between polymer chains.[49] Here, we chose a vesicle formed at $c_{JP} = 0.03$ and $f_A = 0.3$ as the initial state, and reduced the interaction parameter a_{BB} between hydrophobic blocks (denoted by B) from 25 to $25 - \Delta a$, where Δa is a positive value. This change may correspond to an increase in temperature for PNIPAAm, which can swell at lower temperatures and shrink at higher temperatures.[48]

Fig. 7a shows some representative snapshots taken at various simulation times t for vesicles formed at $\Delta a = 2.5$ and $\Delta a = 5.0$, respectively. For both systems, pores in the vesicle walls were observed and could exist during the full course of simulations (note that such pores do not appear at $\Delta a = 0$). These pores are thermodynamically stable due to the arrangement of Janus nanoparticles at the edges (see the insets of Fig. 7b and c), which prevents the hydrophobic blocks from contacting with the solvents. The size of pores formed at $\Delta a = 5.0$ is around four times larger than those formed at $\Delta a = 2.5$, and can accommodate more solvents within it (see the density profiles shown in Fig. 7b and c). Furthermore, we can both start from an intact vesicle to achieve perforated ones by changing a_{BB} from 25 to $25 - \Delta a$, and reversely start from a perforated one to achieve an intact vesicle by resetting a_{BB} to 25. All these observations suggest the controllability of these pores and indicate a novel method to produce polymersomes with "breathable" membranes.

Stability region diagram. As stated in the last two subsections, the incorporation of Janus nanoparticles into the "star-like" aggregates formed by copolymers with $f_A = 0.5$ and the "crew-cut" aggregates formed by copolymers with $f_A = 0.3$ resulted in different morphological changes. In order to systematically elucidate the stability regions of nanostructures, we constructed a two-dimensional diagram in the space of the copolymer composition (f_A) and the particle volume fraction (c_{JP}), which is shown in Fig. 8. In this figure, four regions are identified, which correspond to the spherical micelles (denoted by S), the rod-like micelles (denoted by R), the vesicles (denoted by V), and the mixtures of spherical and rod-like micelles (denoted by S + R), respectively. Note that the R region is actually corresponding to the interconnected networks. For the ABPs with $f_A \leq 0.2$, the hydrophilic blocks are too short to shield the hydrophobic blocks from the solvents. As a result, large compound micelles are formed (not shown in this figure). For the ABPs with $0.3 \leq f_A \leq 0.4$, vesicles are constantly formed. For the symmetric copolymers with $f_A = 0.5$, a morphological transition of S + R → R → V with increasing c_{JP} can

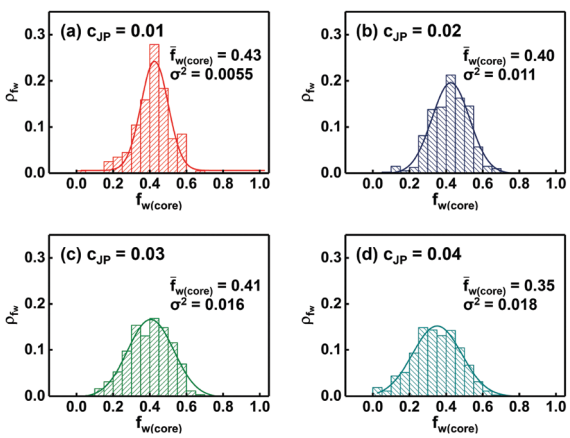

Fig. 6 Volume fractions $\rho_{fw(core)}$ of JPs with various $f_{w(core)}$ within hybrid vesicles formed at different c_{JP}: (a) $c_{JP} = 0.01$; (b) $c_{JP} = 0.02$; (c) $c_{JP} = 0.03$; (d) $c_{JP} = 0.04$. Composition of ABPs was fixed to be $f_A = 0.3$. Solid lines represent the best-fitted Gaussians. Number-average wrapping fraction $\bar{f}_{w(core)}$ and variance σ^2 are displayed.

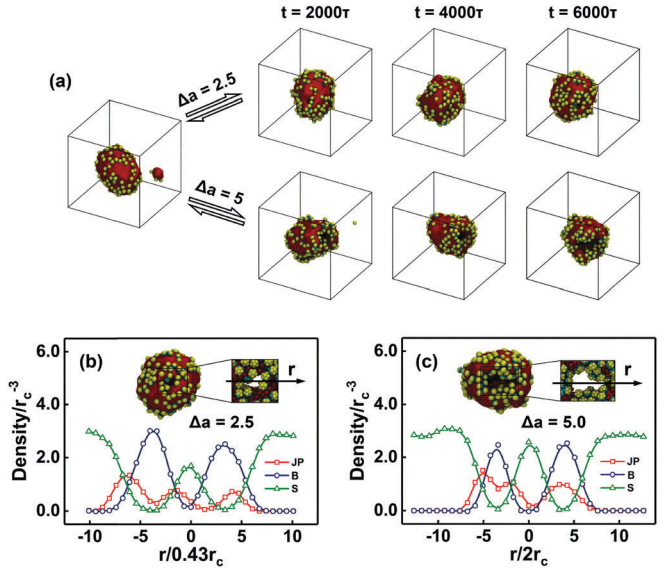

Fig. 7 (a) Morphologies of vesicles formed at different Δa (top: Δa = 2.5; down: Δa = 5.0). Initial structure of both systems is shown at the left side. Volume fraction c_{JP} of nanoparticles is equal to 0.03. Snapshots were taken sequentially at different time t (denoted above each column). τ is the time unit in DPD simulations. (b and c) Density profiles of respective components along the r-arrows for vesicles formed at (b) Δa = 2.5 and (c) Δa = 5.0. Inset of each panel shows the magnification of a representative pore within the vesicle wall. Density profiles of hydrophilic blocks are omitted for clarity.

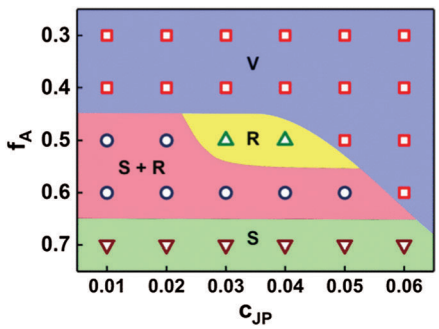

Fig. 8 Stability regions of JP/ABP nanostructures in dilute solutions as the functions of f_A and c_{JP}. Notations S, R, V and S + R correspond to the spherical micelles, rod-like micelles, vesicles and the mixtures of spherical and rod-like micelles, respectively. Regions are denoted by different colours.

be observed. For f_A = 0.6, a morphological transition from S + R → V can be triggered by the increase in c_{JP}. The absence of networks is due to the steric effect of the longer hydrophilic blocks. For the ABPs with f_A = 0.7, the size of hydrophilic blocks is so large that only spheres can exist. For $f_A > 0.7$, the systems are in disorder states.

Moreover, the influence of the composition of copolymers on the morphologies of aggregates can also be viewed from this diagram. At both low and high c_{JP} regions, increasing the length of hydrophilic blocks induces morphological transitions from "crew-cut" to "star-like" aggregates. These changes can be attributed to the decreased repulsive interaction of hydrophilic blocks as well as the transition of the shape of copolymers (from cylindrical shape to cone-like shape).[43] Specifically, we observed the formation of interconnected networks at the middle c_{JP} region, which can be explained in terms of the reduced repulsion among hydrophilic blocks, as well as the decreased surface tension which favours the formation of aggregates with a large interface area (see Section 3.1). The appearance of networks at intermediate f_A and c_{JP} regions implies a possible strategy to produce nanoparticle/block copolymer hybrid gels.

Finally, we wish to highlight the significance of our simulation results. Currently, the co-assembly of nanoparticles and block copolymers in solution has been recognized as a promising strategy for the design and preparation of novel nanomaterials.[25] The resulted aggregates have found applications in many fields, such as drug delivery systems and magnetic resonance imaging.[11] In the present work, we studied the self-assembly behaviour of Janus nanoparticle/amphiphilic block copolymer mixtures in selective solvents, and found that the morphologies and structures of hybrid aggregates can be well controlled by tuning the composition of block copolymers and the nanoparticle loadings. These findings could deepen our understanding on the self-assembly of Janus nanoparticles and amphiphilic block copolymers in solution, and offer strategies to produce JP/ABP hybrid nanostructures in selective solvents.

Furthermore, in the present study, the possibility of preparing "breathable" nanoreactors based on JP/ABP hybrid vesicles was also exploited. During the past few years, nanoreactors based on the polymersomes have become an attractive research field. Compared to liposomes, the polymersomes exhibit better stability, flexibility and functionality.[48] By integrating proteins (*e.g.*, channel proteins,[50] receptors[51] and pumping proteins[52]) or incorporating environmentally responsive polymers (such as temperature-sensitive PNIPAAm[53] and pH-sensitive PSBA[54]) into the vesicle walls, these nanoreactors can be engineered to allow for the translocation of agents across the membranes. However, the transmembrane traffic of agents with a large size, such as nanoparticles, polymers with high molecular weight, proteins and DNA double-helix chains, remains a challenge. In the present work, we found that controllable pores in the JP/ABP vesicle walls could be created by changing the interaction parameters between the hydrophobic blocks, which can be related to applying external stimuli in experiments. These pores were thermodynamically stable due to the arrangement of Janus nanoparticles at the edges. In addition, we found that the creation of pores is a reversible process, and their size can be adjusted by tuning the magnitude of the change in interaction parameters. Therefore, we expect that our method is also suitable for real nanoreactors. By incorporating cross-linked PNIPAAm or other stimuli-responsive copolymers into the vesicle walls and changing the temperature or other parameters to induce an internal stress, controllable pores with different areas can be created in the vesicle walls. These pores may allow for the translocation of agents with different sizes (such as nanoparticles, DNA strands, or drug molecules) across the membranes of nanoreactors.

4. Conclusions

DPD simulations were conducted to study the self-assembly behaviour of JP/ABP mixtures in dilute solution. For symmetric ABPs with comparable hydrophilic and hydrophobic block lengths, the mixtures can experience a morphological transition from the dispersed spheres and rods to the networks and to the vesicles as the volume fraction c_{JP} of JPs increases. The particles are distributed at the core–corona interfaces at low c_{JP}, and are shifted towards the coronas to minimize the interfacial energy. The shift becomes stronger as c_{JP} rises, due to the increased contact probability of nanoparticles and the larger curvature of interfaces at higher c_{JP}. The volumes of dispersed micelles and connected networks are in different ranges, and the stability regions of different morphologies can be identified based on the number-average volume of aggregates. On the other hand, the JPs and asymmetric ABPs with shorter hydrophilic blocks constantly form vesicles. At low c_{JP}, the particles are distributed at the core–corona interfaces. The shift of particles within the vesicles is weaker than those within the spherical and rod-like micelles. At high particle loadings, bilayer-like structures of particles are formed within the vesicle walls. The hybrid vesicles can be responsive to external stimuli. By tuning the interaction parameters between hydrophobic blocks, controllable pores in the vesicle walls can be created. Finally, a two-dimensional diagram as a function of the block copolymer composition and the particle loading was constructed to indicate the stability regions of nanostructures. The regions corresponding to the mixtures of spherical and rod-like micelles (denoted by S + R), the networks (R), the vesicles (V), and the spheres (S) were identified. We wish the present work not only throw light upon the self-assembly behaviour of JP/ABP mixtures, but also offers a novel strategy for the design of nanoreactors with selectively permeable membranes.

Conflicts of interest

There are no conflicts of interest to declare.

Acknowledgements

This work was supported by the National Natural Science Foundation of China (No. 21234002 and 21474029). Support from Projects of Shanghai municipality (No. 16520721900 and 14DZ2261205) and the Fundamental Research Funds for the Central Universities (222201714042) is also appreciated.

References

1 X. Gao, Y. Cui, R. M. Levenson, L. W. K. Chung and S. Nie, *Nat. Biotechnol.*, 2004, **22**, 969–976.
2 D. Maysinger, J. Lovrić, A. Eisenberg and R. Savić, *Eur. J. Pharm. Biopharm.*, 2007, **65**, 270–281.
3 L. E. Euliss, S. G. Grancharov, S. O'Brien, T. J. Deming, G. D. Stucky, C. B. Murray and G. A. Held, *Nano Lett.*, 2003, **3**, 1489–1493.
4 J.-F. Berret, N. Schonbeck, F. Gazeau, D. El Kharrat, O. Sandre, A. Vacher and M. Airiau, *J. Am. Chem. Soc.*, 2006, **128**, 1755–1761.
5 S. Lecommandoux, O. Sandre, F. Chécot, J. Rodriguez-Hernandez and R. Perzynski, *Adv. Mater.*, 2005, **17**, 712–718.
6 N. Nasongkla, E. Bey, J. Ren, H. Ai, C. Khemtong, J. S. Guthi, S.-F. Chin, A. D. Sherry, D. A. Boothman and J. Gao, *Nano Lett.*, 2006, **6**, 2427–2430.
7 Y. Mai and A. Eisenberg, *Macromolecules*, 2011, **44**, 3179–3183.
8 W. Li, S. Liu, R. Deng and J. Zhu, *Angew. Chem., Int. Ed.*, 2011, **50**, 5865–5868.
9 Y. Liu, J.-J. Yin and Z. Nie, *Nano Res.*, 2014, **7**, 1719–1730.
10 C. Sanson, O. Diou, J. Thévenot, E. Ibarboure, A. Soum, A. Brûlet, S. Miraux, E. Thiaudière, S. Tan, A. Brisson, V. Dupuis, O. Sandre and S. Lecommandoux, *ACS Nano*, 2011, **5**, 1122–1140.
11 Y. Mai and A. Eisenberg, *Acc. Chem. Res.*, 2012, **45**, 1657–1666.
12 C. Yang, Q. Li, C. Cai and J. Lin, *Langmuir*, 2016, **32**, 6917–6927.
13 R. J. Hickey, A. S. Haynes, J. M. Kikkawa and S.-J. Park, *J. Am. Chem. Soc.*, 2011, **133**, 1517–1525.
14 A. Walther and A. H. E. Müller, *Chem. Rev.*, 2013, **113**, 5194–5261.
15 M. A. Fernandez-Rodriguez, Y. Song, M. Á. Rodríguez-Valverde, S. Chen, M. A. Cabrerizo-Vilchez and R. Hidalgo-Alvarez, *Langmuir*, 2014, **30**, 1799–1804.
16 X. Li, L. Zhou, Y. Wei, A. M. El-Toni, F. Zhang and D. Zhao, *J. Am. Chem. Soc.*, 2014, **136**, 15086–15092.
17 L. Zhang, Y. Chen, Z. Li, L. Li, P. Saint-Cricq, C. Li, J. Lin, C. Wang, Z. Su and J. I. Zink, *Angew. Chem., Int. Ed.*, 2016, **55**, 2118–2121.
18 S. Hwang, K.-H. Roh, D. W. Lim, G. Wang, C. Uher and J. Lahann, *Phys. Chem. Chem. Phys.*, 2010, **12**, 11894–11899.
19 J. Zhang, E. Luijten and S. Granick, *Annu. Rev. Phys. Chem.*, 2015, **66**, 581–600.
20 A. A. Shah, B. Schultz, W. Zhang, S. C. Glotzer and M. J. Solomon, *Nat. Mater.*, 2015, **14**, 117–124.
21 H. Liu, C.-H. Hsu, Z. Lin, W. Shan, J. Wang, J. Jiang, M. Huang, B. Lotz, X. Yu, W.-B. Zhang, K. Yue and S. Z. D. Cheng, *J. Am. Chem. Soc.*, 2014, **136**, 10691–10699.
22 Q. Chen, S. C. Bae and S. Granick, *Nature*, 2011, **469**, 381–384.
23 Z. Xu, J. Lin, Q. Zhang, L. Wang and X. Tian, *Polym. Chem.*, 2016, **7**, 3783–3811.
24 S. Riniker, J. R. Allison and W. F. van Gunsteren, *Phys. Chem. Chem. Phys.*, 2012, **14**, 12423–12430.
25 Q. Zhang, J. Lin, L. Wang and Z. Xu, *Prog. Polym. Sci*, DOI: 10.1016/j.progpolymsci.2017.04.003.
26 X. Wan, T. Gao, L. Zhang and J. Lin, *Phys. Chem. Chem. Phys.*, 2017, **19**, 6707–6720.
27 L. Zhang, J. Lin and S. Lin, *Macromolecules*, 2007, **40**, 5582–5592.
28 R. B. Thompson, V. V. Ginzburg, M. W. Matsen and A. C. Balazs, *Science*, 2001, **292**, 2469–2472.
29 C.-Y. Li, M.-B. Luo, J.-H. Huang and H. Li, *Phys. Chem. Chem. Phys.*, 2015, **17**, 31877–31886.

30 L. Wang, H. Liu, F. Li, J. Shen, Z. Zheng, Y. Gao, J. Liu, Y. Wu and L. Zhang, *Phys. Chem. Chem. Phys.*, 2016, **18**, 27232–27244.
31 R. D. Groot and P. B. Warren, *J. Chem. Phys.*, 1997, **107**, 4423–4435.
32 L.-T. Yan, N. Popp, S.-K. Ghosh and A. Böker, *ACS Nano*, 2010, **4**, 913–920.
33 B. Dong, Z. Huang, H. Chen and L.-T. Yan, *Macromolecules*, 2015, **48**, 5385–5393.
34 P. Chen, Y. Yang, B. Dong, Z. Huang, G. Zhu, Y. Cao and L.-T. Yan, *Macromolecules*, 2017, **50**, 2078–2091.
35 S. Jury, P. Bladon, M. Cates, S. Krishna, M. Hagen, N. Ruddock and P. Warren, *Phys. Chem. Chem. Phys.*, 1999, **1**, 2051–2056.
36 T. Murtola, A. Bunker, I. Vattulainen, M. Deserno and M. Karttunen, *Phys. Chem. Chem. Phys.*, 2009, **11**, 1869–1892.
37 T. Jiang, L. Wang, S. Lin, J. Lin and Y. Li, *Langmuir*, 2011, **27**, 6440–6448.
38 T. Jiang, L. Wang and J. Lin, *Langmuir*, 2013, **29**, 12298–12306.
39 C. Cai, L. Wang, J. Lin and X. Zhang, *Langmuir*, 2012, **28**, 4515–4524.
40 B. Wang, B. Li, B. Zhao and C. Y. Li, *J. Am. Chem. Soc.*, 2008, **130**, 11594–11595.
41 A. Walther, K. Matussek and A. H. E. Müller, *ACS Nano*, 2008, **2**, 1167–1178.
42 X. Zhang, L. Wang, L. Zhang, J. Lin and T. Jiang, *Langmuir*, 2015, **31**, 2533–2544.
43 Y. Mai and A. Eisenberg, *Chem. Soc. Rev.*, 2012, **41**, 5969–5985.
44 B. Dong, R. Guo and L.-T. Yan, *Macromolecules*, 2014, **47**, 4369–4379.
45 Y. Hirose, S. Komura and Y. Nonomura, *J. Chem. Phys.*, 2007, **127**, 054707.
46 R. Shimizu and H. Tanaka, *Nat. Commun.*, 2015, **6**, 7407.
47 L. Wang, J. Lin and X. Zhu, *RSC Adv.*, 2012, **2**, 12870–12878.
48 J. Gaitzsch, X. Huang and B. Voit, *Chem. Rev.*, 2016, **116**, 1053–1093.
49 Z. Zhuang, T. Jiang, J. Lin, L. Gao, C. Yang, L. Wang and C. Cai, *Angew. Chem., Int. Ed.*, 2016, **55**, 12522–12527.
50 M. Kumar, J. E. O. Habel, Y.-X. Shen, W. P. Meier and T. Walz, *J. Am. Chem. Soc.*, 2012, **134**, 18631–18637.
51 A. Graff, M. Sauer, P. Van Gelder and W. Meier, *Proc. Natl. Acad. Sci. U. S. A.*, 2002, **99**, 5064–5068.
52 H.-J. Choi and C. D. Montemagno, *Nano Lett.*, 2005, **5**, 2538–2542.
53 Q. Yan, J. Wang, Y. Yin and J. Yuan, *Angew. Chem., Int. Ed.*, 2013, **52**, 5070–5073.
54 P. Tanner, S. Egli, V. Balasubramanian, O. Onaca, C. G. Palivan and W. Meier, *FEBS Lett.*, 2011, **585**, 1699–1706.